Aalborg Universitet

AALBORG UNIVERSITY

Synchronization Stability of Interconnected Microgrids with Fully Inverter-based Distributed Energy Resources

Naderi, Mobin; Shafiee, Qobad; Blaabjerg, Frede; Bevrani, Hassan

Published in:
Journal of Modern Power Systems and Clean Energy

DOI (link to publication from Publisher):
10.35833/MPCE.2022.000594

Creative Commons License
CC BY 4.0

Publication date:
2023

Document Version
Publisher's PDF, also known as Version of record

Link to publication from Aalborg University

Citation for published version (APA):
Naderi, M., Shafiee, Q., Blaabjerg, F., & Bevrani, H. (2023). Synchronization Stability of Interconnected Microgrids with Fully Inverter-based Distributed Energy Resources. *Journal of Modern Power Systems and Clean Energy*, *11*(4), 1257-1268. https://doi.org/10.35833/MPCE.2022.000594

General rights
Copyright and moral rights for the publications made accessible in the public portal are retained by the authors and/or other copyright owners and it is a condition of accessing publications that users recognise and abide by the legal requirements associated with these rights.

- Users may download and print one copy of any publication from the public portal for the purpose of private study or research.
- You may not further distribute the material or use it for any profit-making activity or commercial gain
- You may freely distribute the URL identifying the publication in the public portal -

Take down policy
If you believe that this document breaches copyright please contact us at vbn@aub.aau.dk providing details, and we will remove access to the work immediately and investigate your claim.

Downloaded from vbn.aau.dk on: May 12, 2026

Synchronization Stability of Interconnected Microgrids with Fully Inverter-based Distributed Energy Resources

Mobin Naderi, Qobad Shafiee, *Senior Member*, *IEEE*, Frede Blaabjerg, *Fellow*, *IEEE*, and Hassan Bevrani, *Senior Member*, *IEEE*

***Abstract*—In this paper, the synchronization stability challenges of same-rated frequency interconnected microgrids (IMGs) with fully inverter-based generation units are studied. In this type of weak power grid with low *X*/*R* ratios and low line impedances, no strong source with a high-inertia rating exists with which other generation units can be synchronized. Two IMGs controlled using a pinning consensus-based control architecture are considered. The inrush power flow at the beginning of the interconnection process is modeled and analyzed. This power flow is affected by the voltage/phase/frequency difference of the IMG points of common coupling. A small-signal model of the IMGs is obtained that includes a synchronization control unit, and small-signal stability is analyzed based on sensitivity analysis of the most important control and operational parameters. In addition, the transient stability of a nonlinear model of the IMGs under study as implemented in SimPowerSystems/MATLAB is investigated. Stable synchronization is more challenging than the synchronization of multi-area strong power grids and grid-connected MGs. However, synchronization can still be performed by selecting more limited ranges for the control gains and threshold values of the synchronization algorithm. Nevertheless, different disturbances such as high load conditions can cause synchronization instability.**

***Index Terms*—Inrush power, interconnected microgrid, synchronization, small-signal stability, transient stability.**

I. Introduction

MICROGRIDS (MGs) consist of a set of distributed energy resources (DERs) and consumers. MGs can be operated in islanded, grid-connected, and interconnected modes using appropriate control architectures. Interconnected MGs (IMGs) provide a more flexible, reliable, sustainable, and resilient operational mode [1], [2]. AC IMGs can be operated synchronously at the same frequency or asynchronously at different frequencies. The first is performed using circuit breakers (CBs) [3]-[7] or static switches [8], and the second is conducted using back-to-back converters [9]-[11] as interconnection devices. Although synchronization is not a challenge in asynchronous IMGs because of the DC links between them, it remains a critical issue in synchronous IMGs. In particular, in IMGs with fully inverter-based DERs, no strong and high-inertia grid-forming DER or MG exists to provide a stiff grid with which other DERs can be synchronized. This is in contrast to conventional power systems.

Synchronization is defined as a process that minimizes differences in voltage magnitude, phase angle, and frequency between a voltage source or a current source and an active grid [12]. Power plants, DERs, and MGs can be examples of voltage and current sources. Several synchronization methods are currently used, including passive, active, open transition, and measurement-free strategies [12], [13]. The synchronization process can be categorized into two types according to grid-feeding and grid-forming DERs, that is the synchronization of current and voltage sources, respectively. Grid-feeding DERs as current sources generally synchronize with the grid using phase-locked loops [12], [14], whereas a more complete synchronization control unit is required for grid-forming DERs and the islanded MGs as voltage sources to minimize voltage, phase angle, and frequency differences prior to connect to the power grid [15]. The latter derives from existing individual voltage and frequency controllers in both sides of synchronization.

On the other hand, the synchronization challenges are different for large grid-forming power plants connected to high-voltage stiff power systems [16] as well as for grid-forming DERs and MGs connected to low- or medium-voltage stiff grids [13], [15] and for weak MGs interconnected without existing stiff grids [17]. In the first case, the grid is considerably stiff because of the presence of many high-rated power rotational power plants and because of a high-*X*/*R* ratio and low line impedances. Therefore, a reliable and resilient reference exists for the synchronization of grid-connected generation units. In the second case, although the distribution grid is not stiff, its power rating is much higher than the nominal power of the DERs and MGs at the point of common coupling (PCC). Thus, it can still be considered an infinite bus with which a DER/MG can be synchronized. In the third case, not only does no high-rated high-*X*/*R* grid exist, but al-

Manuscript received: September 14, 2022; revised: October 13, 2022; accepted: November 12, 2022. Date of CrossCheck: November 12, 2022. Date of online publication: January 10, 2023.

This article is distributed under the terms of the Creative Commons Attribution 4.0 International License (http://creativecommons.org/licenses/by/4.0/).

M. Naderi (corresponding author), Q. Shafiee, and H. Bevrani are with the Smart/Micro Grids Research Center (SMGRC), University of Kurdistan, Sanandaj, Iran (e-mail: m.naderi@eng.ac.ir; q.shafiee@uok.ac.ir; bevrani@uok.ac.ir).

F. Blaabjerg is with Department of Energy Technology, Aalborg University, Aalborg, Denmark (e-mail: fbl@energy.aau.dk).

DOI: 10.35833/MPCE.2022.000594

so most of the DERs in the MGs are non-rotary converter-based. In this case, synchronization stability is very challenging.

In single MGs under a strong grid, synchronization control is presented for seamless transition from islanded to grid-connected mode [18]-[25], where a strong grid should be an ideal voltage source (infinite bus). In [19], [21], and [24], small-signal stability is analyzed but synchronization-related parameters are not considered. Robust and model predictive controllers are employed to improve the seamless transition [25]. The synchronization process is developed for multi-bus MGs using a leader-follower control strategy [24] and multi-master and multi-slave MGs [26]. The synchronization controller gains are optimized to decrease the inrush current [20], where the threshold values of the voltage, phase, and frequency differences of the MG PCCs and the power grid are considered to be 3%, 1°, and 0.05 Hz, respectively. To synchronize the DERs and MGs for a rated capacity of less than 500 kVA to the utility grid, IEEE Standard 1547-2003 recommends synchronization criteria for voltage, phase, and frequency differences of ±10%, 20°, and 0.3 Hz, respectively [27].

In IMG research, [28] focuses on the transition mode of forming IMGs and presents the logic control required for synchronization and interconnection by static switches. In addition, a transient stability criterion is proposed as the time required for successful synchronization for different frequency and phase differences on IMG PCCs. Seamless transition of IMGs is discussed in [29]. Furthermore, a fuzzy-based droop controller [30] and an adaptive control scheme [17] are used to enhance the transient response.

This paper performs a stability analysis of the synchronization of weak IMGs with fully inverter-based DERs. Both small-signal and transient analyses are conducted, as these have not been previously addressed [17], [28]-[30]. The contributions of this paper are described as follows.

The inrush power at the beginning of the MG interconnection is modeled and analyzed while considering the specifications of weak IMGs. The most effective parameters for the inrush power are studied, and the transition from inrush power to scheduled power is discussed.

A small-signal model of the synchronization control unit adopted from [19], [20], and [24] is proposed, and small-signal stability of IMGs, with a focus on the parameters affecting the synchronization process (i. e., synchronization and secondary controller parameters), is assessed.

The transient stability of IMG synchronization is analyzed by using time-domain simulations and considering the synchronization constraint thresholds and effects of disturbance length to investigate the challenges inherent in a complete synchronization process.

The remainder of this paper is organized as follows. The analysis of inrush power between IMGs is discussed in Section II. Section III reviews the control requirements of synchronous MGs. Small-signal modeling and stability analysis are presented in Section IV. Transient stability is assessed in Section V. Section VI concludes the paper. Note that the data source files considered in Sections II and IV are available in [31].

II. Analysis of Inrush Power Between IMGs

Figure 1(a) illustrates the MG connections through CBs and interlinking lines. They are synchronous because they operate at the same frequency after the CBs are closed and synchronization transients are completed. A typical structure of MGs is investigated in this paper, which is shown in Fig. 1(b) for the n^{th} MG, where e_m is the voltage reference of the voltage source inverter (VSI). Each DER_m can generate power up to its rated power. After the voltage v_{om} and current i_{lm} are filtered using an inductor-capacitor (LC) filter with inductance L_{fm}, resistance R_{fm}, and capacitance C_{fm}, the power flows via a coupling line with inductance $L_{li,m}$ and resistance $R_{li,m}$ to the MG PCC, denoted by the voltage $v_{pcc,n}$. Both local and remote loads can be supplied. They are considered as lumped loads at the PCC, i.e., the resistance R_{lo}^n in series with inductance L_{lo}^n. Interconnections are established among the MGs at the PCCs. MGs can be operated either independently or in an interconnected manner using the coordination control to share power. Note that in Fig. 1, i_{IL}^{12} is the current of interlinking line between MG_1 and MG_2, and i_{IL}^{ns} is the current of interlinking line between MG_n and MG_s.

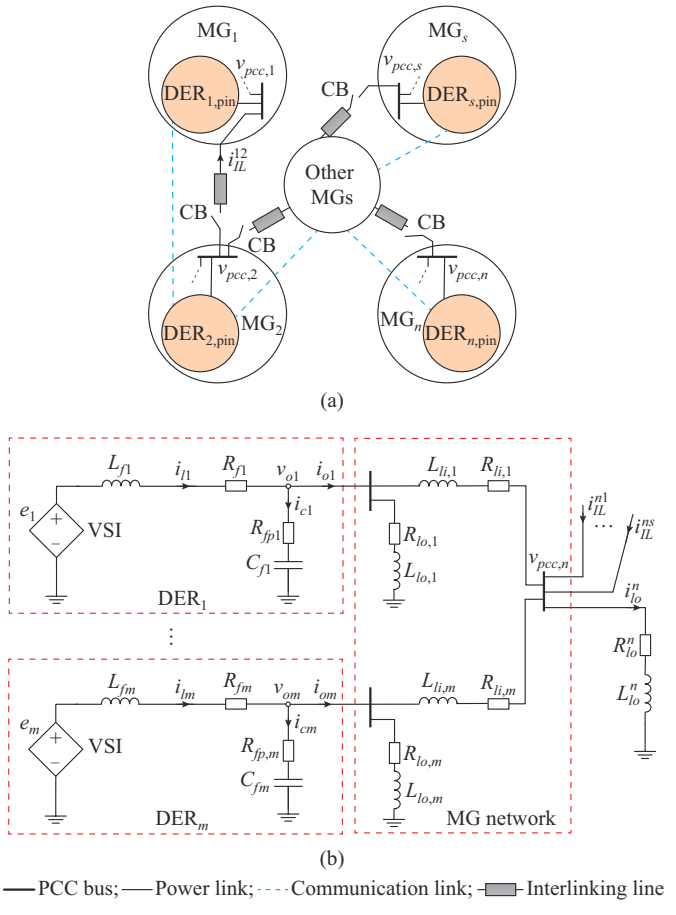

Fig. 1. Synchronous IMGs. (a) MG connections through CBs and interlinking lines. (b) MG power parts, including VSIs, LC filters, coupling lines, and loads.

A. Modeling of Inrush Power

Figure 2 shows simple schematic of two synchronous MGs with a focus on PCCs of MG_1 and MG_2 and interlink-

ing line between them. No synchronization process exists for observing the true effect of the voltage magnitude/phase/frequency difference on the inrush power at the interconnection instance. This is also crucial at the beginning of the synchronization process, as pre-synchronization may result in nonzero differences. Therefore, the inrush power at the beginning of synchronization, i.e., interconnection instance, is strongly influenced by the voltage magnitude/phase/frequency difference. However, after a brief period, the differences are limited to zero because of synchronization control efforts. In the steady state, the synchronization control loop is open and the power exchange between the MGs is fully controlled by the secondary controllers of the leader DER that share IMG loads.

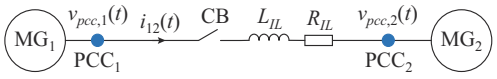

Fig. 2. Simple schematic of two synchronous MGs with a focus on PCCs of MG_1 and MG_2 and interlinking line between them.

Considering the single-phase equivalent circuit of the interconnection shown in Fig. 2 when using Kirchhoff voltage law, we can obtain:

$$R_{IL} i_{12}(t) + L_{IL} \frac{\mathrm{d}i_{12}(t)}{\mathrm{d}t} = v_{pcc,1}(t) - v_{pcc,2}(t) \tag{1}$$

where R_{IL} and L_{IL} are the resistance and inductance of the interlinking line, respectively; and $i_{12}(t)$ is the single-phase current from MG_1 to MG_2. Assuming sinusoidal voltages as $v_{pcc,1}(t) = V_{p1}\sin(\omega_1 t + \phi_{pcc,1})$ and $v_{pcc,2}(t) = V_{p2}\sin(\omega_2 t + \phi_{pcc,2})$ and considering their corresponding solutions as $i_{12,pr1}(t) = I_{pr1}\sin(\omega_1 t + \theta_1)$ and $i_{12,pr2}(t) = I_{pr2}\sin(\omega_2 t + \theta_2)$, we can solve (1) and find the complete solution as:

$$i_{12}(t) = (I_{pr2}\sin(\theta_2) - I_{pr1}\sin(\theta_1))\mathrm{e}^{-(R/L)t} + i_{12,pr1}(t) - i_{12,pr2}(t) \tag{2}$$

where I_{pr1}, I_{pr2}, θ_1, and θ_2 are obtained using the superposition principle and by replacing $i_{12,pr1}(t)$ and $i_{12,pr2}(t)$ in (1), respectively, with:

$$\begin{cases} I_{pr1} = \dfrac{V_{p1}}{\sqrt{R_{IL}^2 - (\omega_1 L_{IL})^2}} \\ I_{pr2} = \dfrac{V_{p2}}{\sqrt{R_{IL}^2 - (\omega_2 L_{IL})^2}} \end{cases} \tag{3}$$

$$\begin{cases} \theta_1 = \phi_1 - \tan^{-1}\left(\dfrac{\omega_1 L_{IL}}{R_{IL}}\right) \\ \theta_2 = \phi_2 - \tan^{-1}\left(\dfrac{\omega_2 L_{IL}}{R_{IL}}\right) \end{cases} \tag{4}$$

The current shown in (1) is true only at the beginning of the CB closing, which is called the inrush current. This derives from the fact that, in real situations, the controllers change the PCC voltages after passing their time constants. The exchanged current then changes. Nevertheless, the controller effects are not modeled in this paper. According to the exponential form of current in (2), no extremum point exists, and thus the maximum current value equals the steady-state amount and is expressed as:

$$I_{inrush} = i_{12,pr1}(t) - i_{12,pr2}(t)\Big|_{t \geq 4L_{IL}/R_{IL}} \tag{5}$$

Finally, by generalizing the voltage and current in a balanced three-phase form, we can obtain the active and reactive inrush power at the PCC_1, respectively, as:

$$P_{inrush} = v_{p1a}(t) i_{12a}(t) + v_{p1b}(t) i_{12b}(t) + v_{p1c}(t) i_{12c}(t) \tag{6}$$

$$Q_{inrush} = \frac{1}{\sqrt{3}}[(v_{p1b}(t) - v_{p1c}(t)) i_{12a}(t) + (v_{p1c}(t) - v_{p1a}(t)) i_{12b}(t) + (v_{p1a}(t) - v_{p1b}(t)) i_{12c}(t)] \tag{7}$$

B. Effects of PCC Voltage Magnitude, Phase, and Frequency Differences on Inrush Power

Figure 3 shows the inrush power values derived from PCC voltage magnitude, phase, and frequency of the PCCs change in probable ranges. Scenario 1 (Fig. 3(a) and (b)) and scenario 2 (Fig. 3(c) and (d)) are considered, where the influencing variables are listed in Table I. In both scenarios, the line resistance and inductance are $R_{IL} = 1.6\ \Omega$ and $L_{IL} = 1.9$ mH, respectively. In addition, the time following the interconnection is selected as $t = 0.15$ s. Studies that address inrush power are considered for stable and uninterruptible operations of IMGs. Therefore, the time value is chosen as a mean value for the detection and operation of CBs in low-voltage power systems.

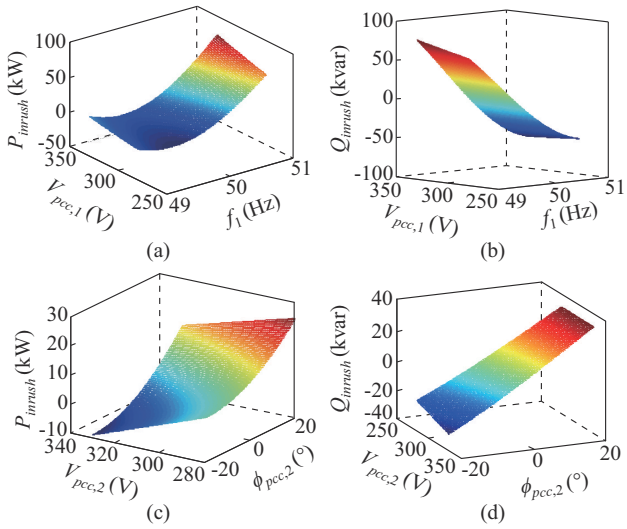

Fig. 3. Inrush power values derived from PCC voltage magnitude, phase, and frequency changes. (a) Active power for 49 Hz $\leq f_1 \leq$ 51 Hz and 280 V $\leq V_{pcc,1} \leq$ 330 V. (b) Reactive power for 49 Hz $\leq f_1 \leq$ 51 Hz and 280 V $\leq V_{pcc,1} \leq$ 330 V. (c) Active power for $-20° \leq \phi_{pcc,2} \leq 20°$ and 280 V $\leq V_{pcc,2} \leq$ 330 V. (d) Reactive power for $-20° \leq \phi_{pcc,2} \leq 20°$ and 280 V $\leq V_{pcc,2} \leq$ 330 V.

TABLE I
VALUES OF INFLUENCING VARIABLES IN INRUSH POWER

Scenario	f_1 (Hz)	$v_{pcc,1}$ (V)	$\phi_{pcc,1}$ (°)	f_2 (Hz)	$v_{pcc,2}$ (V)	$\phi_{pcc,2}$ (°)
Scenario 1	[49, 51]	[280, 330]	5	50	320	0
Scenario 2	50	320	5	50	[280, 330]	[−20, 20]

As Fig. 3(a) shows, the active inrush power increases when $v_{pcc,1}$ and f_1 increase. However, changing the frequency is more effective for the inrush power value. In addition, a

minimum point exists with respect to $f_1=50$ Hz. The reactive inrush power exhibits inverse behavior as f_1 changes, as shown in Fig. 3(b). A symmetry can be observed with changes to f_1, where Q_{inrush} decreases when f_1 increases. In scenario 2, decreasing $v_{pcc,2}$ and increasing $\phi_{pcc,2}$ cause an increase in P_{inrush}, as shown in Fig. 3(c). Q_{inrush} also increases considerably with an increase in $\phi_{pcc,2}$, as shown in Fig. 3(d). In fact, for $\Delta\phi_{pcc}>0$, the reactive inrush power flows from PCC_2 to PCC_1, and vice versa. In general, the effectiveness of the inrush power value derives from the frequency, phase, and voltage magnitude differences, respectively. Unlike in conventional power systems, autonomous IMGs are weak grids, so that there is not a stiff or robust frequency with which other MGs can be synchronized. Therefore, in a synchronization process, each MG suffers from a weak and insecure frequency, where the frequency may vary highly at approximately the nominal value due to disturbances, e.g., sudden load changes. In addition, PCCs may be far from VSI-based DERs to experience large voltage sags and phase shifting, leading to different PCC voltage magnitudes and phases.

C. Effects of X/R Ratio and Impedance Value on Inrush Power

Figure 4 shows the inrush power values for different *X/R* ratios of [0.1, 5]. Three frequency difference values are considered, namely, $\Delta f=-0.1$ Hz, $\Delta f=0$, and $\Delta f=0.1$ Hz. However, the voltage magnitude and phase differences are constant at $\Delta V_{pcc}=5$ V and $\Delta\phi_{pcc}=5°$, respectively. Figure 4(a) and (b) shows that both P_{inrush} and Q_{inrush} increase with an increase in the *X/R* ratio. Yet, for $\Delta f=-0.1$ Hz, varying P_{inrush} is negligible. This is due to the inverse effect of this Δf with respect to ΔV_{pcc} and $\Delta\phi_{pcc}$. Q_{inrush} also shows the most minimal variations at $\Delta f=-0.1$ Hz. Another critical fact is the inverse directions of P_{inrush} and Q_{inrush} for situations under the same signs of Δf, ΔV_{pcc}, and $\Delta\phi_{pcc}$. Finally, for IMGs, which are generally implemented in $X/R<2$, P_{inrush} has the lowest values, whereas Q_{inrush} has the highest values.

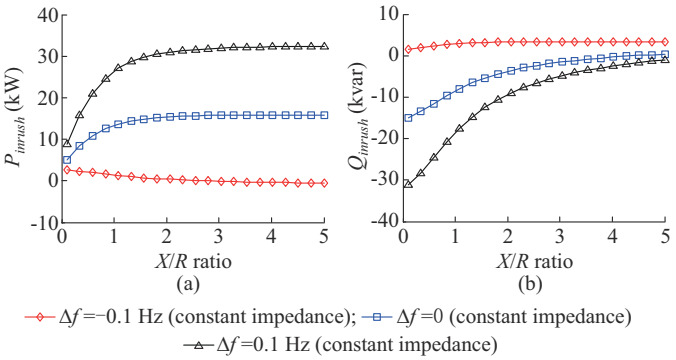

Fig. 4. Inrush power values for different *X/R* ratios of [0.1, 5] when $\Delta V_{pcc}=5$ V and $\Delta\phi_{pcc}=5°$. (a) Active inrush power. (b) Reactive inrush power.

According to typical line data for low-, medium-, and high-voltage power lines [29], decreasing impedance values by increasing the *X/R* ratio is essential. Accordingly, the line impedance is reduced from 0.85 Ω to 0.25 Ω when the *X/R* ratio increases from 0.1 to 5, i.e., from a low- to a high-voltage line. Figure 5 shows inrush power values for simultaneous changes. Most results presented for the constant-impedance scenario are valid under a variable-impedance scenario. However, the rate of power change is higher than that under a constant-impedance scenario because of a decrease in impedance as the *X/R* ratio increases.

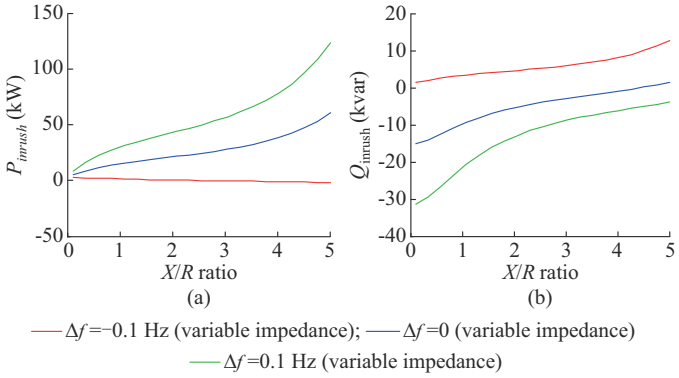

Fig. 5. Inrush power values for simultaneous changes of *X/R* ratio of [0.1, 5] and impedance values of [0.85, 25] when $\Delta V_{pcc}=5$ V and $\Delta\phi_{pcc}=5°$. (a) Active inrush power. (b) Reactive inrush power.

Figure 6 shows the inrush power values for different impedance values of $[0.1, 2.6]\,\Omega$ for the interlinking line. Figure 6(a) and (b) shows that the absolute values of P_{inrush} and Q_{inrush} decrease when the interlinking line impedance increases. Consequently, a virtual impedance can be added at the interconnection instance to limit the inrush power.

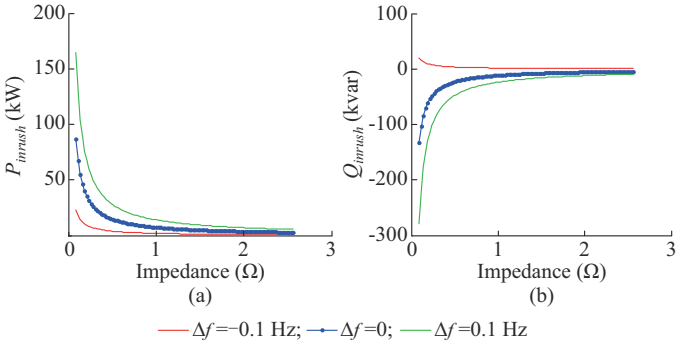

Fig. 6. Inrush power values for different impedance values of $[0.1, 2.6]\,\Omega$ for interlinking line when $\Delta V_{pcc}=5$ V and $\Delta\phi_{pcc}=5°$. (a) Active inrush power. (b) Reactive inrush power.

III. Control Requirements of Synchronous MGs

A. Basic Control Structure

Figure 7 shows the basic control of IMGs, including inner, primary, and secondary controller loops and communication, where the leader and follower DER control loops are separately represented. The inner and primary control units are similar for both DER types. Figure 8 shows the details of the inner control loops of each DER, which consist of a proportional-integral voltage controller with K_{pv} and K_{iv} gains, proportional-integral current controller with K_{pi} and K_{ii} gains, and a virtual inductance L_{vi} loop. The inner voltage and current controllers regulate the voltage v_{od}^m, v_{oq}^m and current i_{ld}^m, i_{lq}^m, respectively, and provide the pulse width mod-

ulation (PWM) unit with the inverter voltage reference e_m to function as a VSI. The primary control unit consists of ω-P and v-Q droop characteristics with k_m^P and k_m^Q gains, where the DER frequency and voltage amplitude references, i. e., ω_m and $v_m^{d,ref}$ are provided to stabilize the frequency and voltage and to share active and reactive power. The virtual inductance loop is used to improve the performances of the ω-P and v-Q droop characteristics in MGs with low X/R ratios of coupling lines.

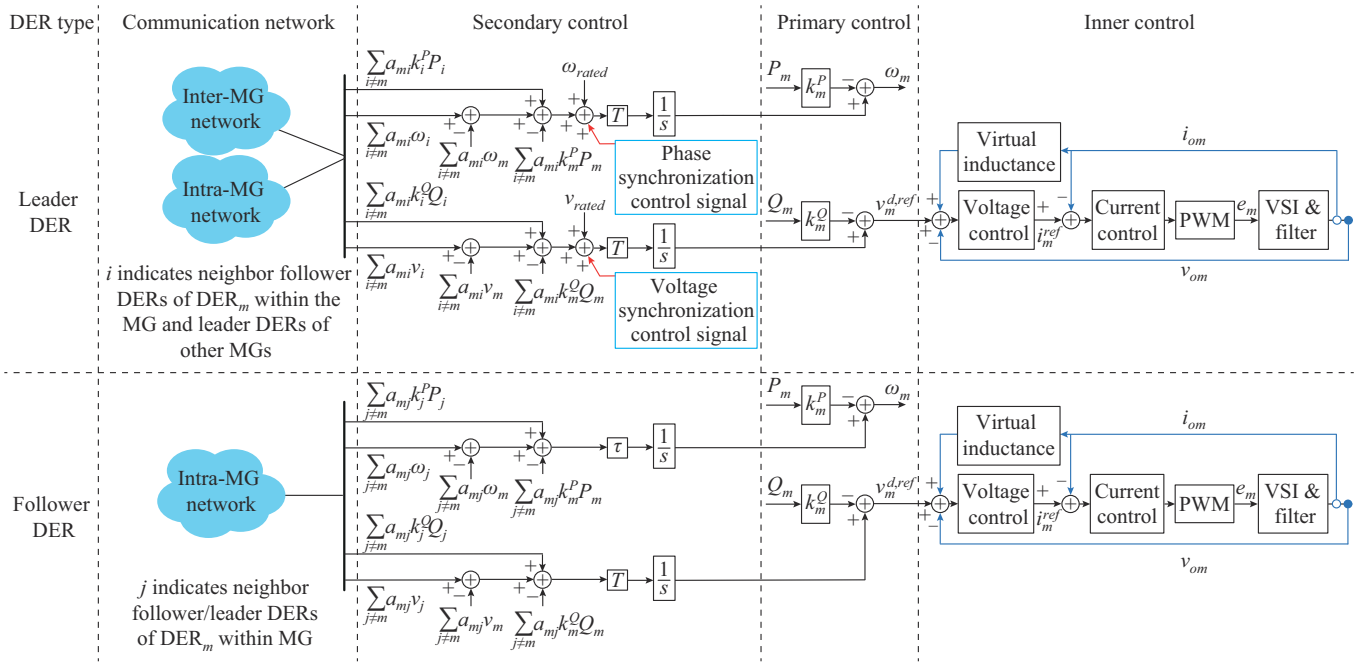

Fig. 7. Basic control of IMGs, including inner, primary, and secondary controller loops and communication.

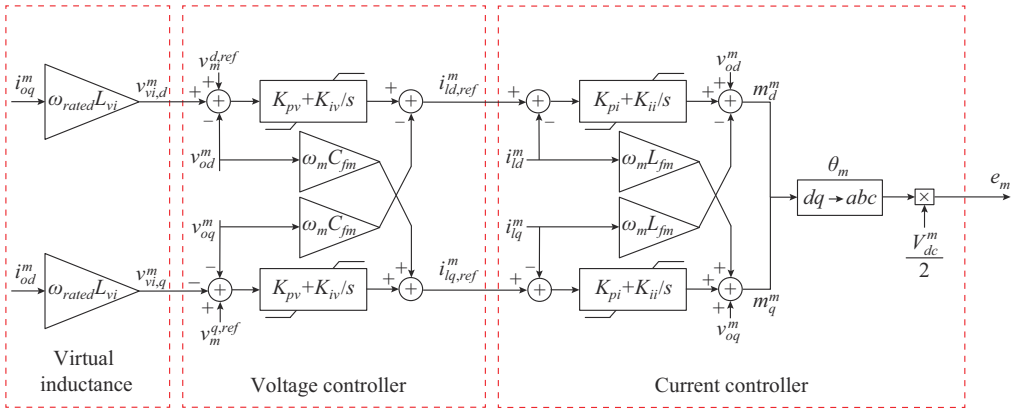

Fig. 8. Details of inner control loops of each DER.

A pinning consensus-based secondary control is selected, in which the control architecture is different for leader and follower DERs [5], [6], [32]-[36]. Two cyber networks are used, namely, inter-MG and intra-MG networks. An inter-MG network is necessary for the synchronism of IMGs and for global power sharing. However, the intra-MG network, i. e., inter-DER network, is used to restore frequency and voltage and improve power sharing in grid-isolated operational modes, i. e., islanded and interconnected modes. MGs are generally considered single-leader and multiple-follower DERs. Only the leader DERs have rated voltage and frequency values. They have two main duties. The first is to communicate power, frequency, and voltage data with other leader DERs in neighboring MGs ($a_{mi}=1$) for controlling overall IMG power sharing during the interconnected operation mode. The second is to communicate the rated voltage and frequency instantaneously with its follower DERs inside the MG ($a_{mi}=1$) to achieve stable intra-MG power sharing and to restore the voltage and frequency to the rated values. Another type of communication is used among neighboring follower DERs ($a_{mj}=1$) to improve power sharing and voltage/frequency restoration in both isolated and interconnected operation modes, which is shown in the bottom row of Fig. 7. Note that the secondary control parameters and variables are explained in [37].

B. Synchronization Control

To connect two MGs in a set of IMGs, synchronizing MG PCCs is necessary. Synchronization is accomplished by

matching the frequencies, PCC voltage phases, and magnitudes. The frequency difference can be considered to be limited to zero due to the frequency restoration performed by the secondary frequency loops with the same rated frequencies. Nevertheless, the phase and magnitude differences in the PCC voltages should be controlled so that they decrease as much as possible, as shown in Fig. 9, where k_{sync} is the synchronization control parameter.

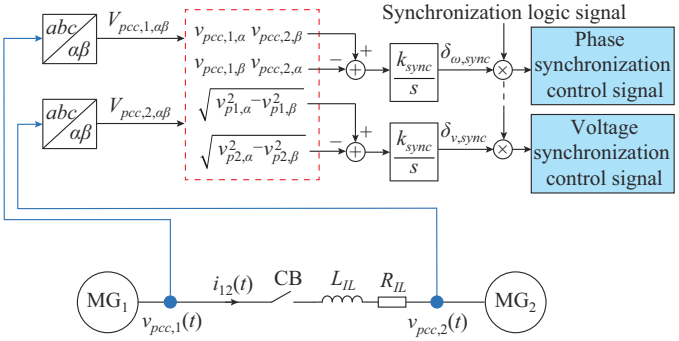

Fig. 9. Synchronization control loop of IMERs with outputs related to Fig. 7.

The lower differences lead to a lower inrush power at the time of interconnection. The PCC voltage phase and magnitude differences of two typical MGs (MG_1 and MG_2) in the $\alpha\beta$ frame are given as follows [19], [20], [24]:

$$\Delta\phi_{pcc}=\phi_{pcc,1}-\phi_{pcc,2}\propto v_{pcc,1,\alpha}v_{pcc,2,\beta}-v_{pcc,1,\beta}v_{pcc,2,\alpha} \tag{8}$$

$$\Delta v_{pcc}=|v_{pcc,1}|-|v_{pcc,2}|=\sqrt{v_{p1,\alpha}^2-v_{p1,\beta}^2}-\sqrt{v_{p2,\alpha}^2-v_{p2,\beta}^2} \tag{9}$$

According to (8) and (9), the difference signals shown in Fig. 8 are used in the synchronization controllers. The controller is selected as an integral type with a small-gain k_{sync} to maintain a stable system. This common synchronization control structure is used to ensure focus remains on stability analysis.

As shown in Fig. 7, the phase synchronization control signal is added to the ω-P error signal of the secondary controller in the leader DER control units. Similarly, the voltage-magnitude synchronization control signal is added to the v-Q error signal. Note that the phase difference control efforts disturb the frequency and lead to a steady-state error during pre-synchronization and synchronization. However, applying it is necessary to achieve lower inrush power.

The synchronization logic signal determines when the synchronization control unit should be affected by the IMG control. In fact, this signal changes from 0 to 1 prior to the interconnection instance, which is the pre-synchronization period. Following the synchronization process, the signal returns to 0. Pre-synchronization is necessary to ensure sufficient time to decrease the phase and voltage differences.

IV. Small-signal Modeling and Stability Analysis

A small-signal model of the IMGs, including the synchronization control loops, is derived. Here, the interconnection method [3], [9] is used.

A. Small-signal Modeling of IMGs

1) Modeling of subsystems: a complete process of small-signal modeling of IMGs interconnected through back-to-back converters (BTBC-IMGs) [9] and interconnected through CBs (CB-IMGs) [3] is already reported by the authors. In order to model IMGs, a list of all subsystems are required, including interlinking lines, MGs, and interlinking devices. With respect to CB-IMGs, the critical subsystems participating in the dominant IMG dynamics are the interlinking lines and MGs that consist of loads, inverter-based DERs and their coupling lines, LC filters, and current, voltage, primary, and secondary controllers. Each subsystem is modeled as an independent module that considers the inputs and outputs from/to other subsystems using a state-space representation [9] as follows:

$$\dot{\boldsymbol{X}}_M(t)=\boldsymbol{A}_M\boldsymbol{X}_M(t)+\boldsymbol{B}_M\boldsymbol{U}_M(t) \tag{10}$$

$$\boldsymbol{Y}_M(t)=\boldsymbol{C}_M\boldsymbol{X}_M(t)+\boldsymbol{D}_M\boldsymbol{U}_M(t) \tag{11}$$

where $\boldsymbol{X}_M(t)$, $\boldsymbol{U}_M(t)$, and $\boldsymbol{Y}_M(t)$ are the module state vector, input vector of all subsystem input signals, and output vector of all subsystem output signals, respectively; and $\boldsymbol{A}_M$, $\boldsymbol{B}_M$, $\boldsymbol{C}_M$, and $\boldsymbol{D}_M$ are the model matrices that should be found for all subsystems. For instance, for the DER coupling line shown in Fig. 1, the inductor currents in the dq frame are the state variables, which are also considered as model outputs, and the voltages of the LC filter and the PCC in the dq frame are used as inputs. The matrices can easily be calculated, as presented in [9], for most subsystems.

2) Modeling of synchronization control unit: the only subsystem of the IMGs under study, which is not modeled, is the synchronization controller that includes two integrators. The integrator outputs are considered as state variables, as shown in Fig. 8. Thus, the state-space representation of each synchronization controller is calculated following a linearization process as:

$$\dot{\boldsymbol{X}}_{sync}(t)=\boldsymbol{A}_{sync}\boldsymbol{X}_{sync}(t)+\boldsymbol{B}_{sync}\boldsymbol{U}_{sync}(t) \tag{12}$$

$$\boldsymbol{Y}_{sync}(t)=\boldsymbol{C}_{sync}\boldsymbol{X}_{sync}(t)+\boldsymbol{D}_{sync}\boldsymbol{U}_{sync}(t) \tag{13}$$

where $\boldsymbol{U}_{sync}=[\Delta v_{p1,dq},\Delta v_{p2,dq},\Delta\omega_{MG1},\Delta\omega_{MG2}]^{\mathrm{T}}$; $\boldsymbol{X}_{sync}=\boldsymbol{Y}_{sync}=[\Delta\delta_{\omega,sync},\Delta\delta_{v,sync}]^{\mathrm{T}}$; $\boldsymbol{A}_{sync}=\boldsymbol{0}_{2\times2}$; $\boldsymbol{C}_{sync}=\boldsymbol{I}_{2\times2}$; $\boldsymbol{D}_{sync}=\boldsymbol{0}_{2\times6}$; and

$$\boldsymbol{B}_{sync}=\boldsymbol{k}_{sync}\begin{bmatrix}\boldsymbol{k}_{p1-\omega} & \boldsymbol{k}_{p2-\omega} & k_{\omega1} & k_{\omega2}\\ \boldsymbol{k}_{p1-v} & \boldsymbol{k}_{p1-v} & 0 & 0\end{bmatrix} \tag{14}$$

where $\boldsymbol{k}_{pi-\omega}=[k_{di-\omega},k_{qi-\omega}]$ and $\boldsymbol{k}_{pi-v}=[k_{di-v},k_{qi-v}]$ for $i=1,2$. In general, k_x, $x\in\{di-\omega,qi-\omega,\omega i\,|\,i=1,2\}$ is obtained by:

$$k_x=\sqrt{a_x^2+b_x^2}\sin(\Delta\omega_{pcc,0}t_0+c_x\pi+d_x\arctan(b_x/a_x)) \tag{15}$$

where $\Delta\omega_{pcc,0}=\omega_{MG1}-\omega_{MG2}$ is the frequency difference at the operating point; and t_0 is the time of inrush power occurrence.

Table II defines a_x, b_x, c_x, and d_x, and the subscripts 0, 1, 2, d, and q refer to the operating point, MG_1, MG_2, direct component of voltage, and quadrature component of voltage, respectively.

TABLE II
PARAMETERS a_x, b_x, c_x, AND d_x OF k_x IN (15)

k_x	a_x	b_x	c_x	d_x
k_{d1}	V_{d20}	V_{q20}	1	−1
k_{q1}	V_{q20}	V_{d20}	1	1
k_{d2}	V_{d10}	V_{q10}	1	1
k_{q2}	V_{q10}	V_{d10}	1	−1
$k_{\omega 1}$	$\omega_{10}(V_{q10}V_{d20}-V_{d10}V_{q20})$	$\omega_{10}(V_{d10}V_{d20}+V_{q10}V_{q20})$	0	−1
$k_{\omega 2}$	$\omega_{20}(V_{d10}V_{q20}-V_{q10}V_{d20})$	$\omega_{20}(V_{d10}V_{d20}+V_{q10}V_{q20})$	0	1

3) Modeling of overall IMGs: to calculate the overall model of IMGs, the subsystem models should be interconnected. With the aim of conducting small-signal stability analysis, this calculation leads to a free-motion state-space model expressed as:

$$\dot{\boldsymbol{X}}_{IMG}(t)=\boldsymbol{A}_{IMG}\boldsymbol{X}_{IMG}(t) \tag{16}$$

where $\boldsymbol{X}_{IMG}(t)$ comprises all state variables of the subsystems; and $\boldsymbol{A}_{IMG}$ is a large state matrix in which the main diagonal arrays include the state matrices of the subsystems that can be calculated numerically as described in [9].

B. Small-signal Stability Analysis

In addition to the synchronization control parameters, the secondary control parameters are also critical in the stability analysis of the synchronization control, as the control signals are applied through the secondary controllers. The MG structure investigated in this paper is shown in Fig. 1(b), where the control requirements are fully considered, as shown in Figs. 7 and 9. The IMG parameters are listed in Table II of [10]. The basic values of the critical parameters and initial values of the PCC voltage and frequency in the stability analysis are presented in Table III, where the subscripts, e.g., leader and follower, and the superscript, e. g., MG, allocate general variables to certain MGs and DERs related to Figs. 7 and 8.

TABLE III
BASIC VALUES OF PARAMETERS AND INITIAL VALUES OF PCC VOLTAGE AND FREQUENCY IN STABILITY ANALYSIS

Parameter	Value	Variable	Initial value
k_{sync}	0.1	f_1, f_2	50 Hz
T	10 s	V_{d10}	310 V
τ	10 s	V_{d20}	310 V
$k_{leader}^{P,MG1}, k_{follower}^{P,MG1}$	15.7×10^{-5}, 7.8×10^{-5}	V_{q10}	−3
$k_{leader}^{Q,MG1}, k_{follower}^{Q,MG1}$	0.006, 0.003	V_{q20}	−3
$k_{leader}^{P,MG2}, k_{follower}^{P,MG2}$	78.6×10^{-5}, 39.3×10^{-5}	K_{pv}, K_{iv}	1, 20
$k_{leader}^{Q,MG2}, k_{follower}^{Q,MG2}$	0.032, 0.016	K_{pi}, K_{ii}	30, 500
L_{vi}	2×10^{-3} H		

1) Synchronization Control Parameter

Figure 10 shows the loci of dominant eigenvalues of IMGs under study, where each MG has one leader DER and one follower DER. k_{sync} varies within [0.01, 1]. In general, the arrows indicate the increasing direction of the parameter. In Fig. 10(a), all PCC voltage and frequency differences are zero. In fact, pre-synchronization is considered to be well performed. Two eigenvalues near the imaginary axis are critical and unstable for $k_{sync}\geq 0.75$. Very low amounts of k_{sync} are not desired. Therefore, intermediate values are appropriate to achieve a better small-signal stability margin. Further analysis can be performed to satisfy the performance objectives such as improved response speed and oscillation damping. Figure 10(b) shows the same loci when $\Delta V_{pcc,d}=-5$ V for circles with solid blue lines and $\Delta V_{pcc,d}=5$ V for stars with red dashed lines. In both situations, IMGs cannot be stable for any value of k_{sync}. This also demonstrates the importance of successful synchronization.

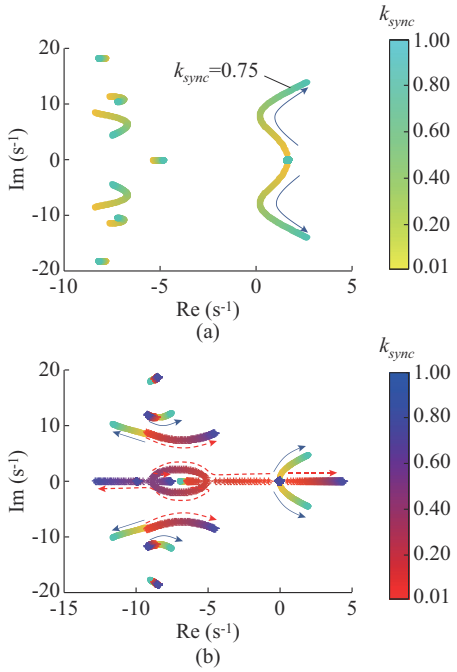

Fig. 10. Loci of dominant eigenvalues of IMGs under study for k_{sync} varying within [0.01, 1]. (a) All PCC voltage and frequency differences are zero. (b) $\Delta V_{pcc,d}=-5$ V for circles and $\Delta V_{pcc,d}=5$ V for stars.

2) Secondary Control Parameters

Figure 11 shows the loci of the most dominant eigenvalues of the IMGs under study when the secondary control parameter of the leader $\text{DER}_{1,1}$ (i.e., T) varies within [0.1, 20].

As Fig. 11(a) shows, the PCC voltage, phase, and frequency differences are zero. Therefore, the stabilizing range of T can be found, which is [5.1, 13.6] s. Nevertheless, in Fig. 11(b), no stabilizing value is shown for $\Delta V_{pcc,d}=-5$ V (circles with blue solid lines), and a small stabilizing range exists for $\Delta V_{pcc,d}=5$ V (stars with red dashed lines).

A condition similar to that shown in Fig. 11 is considered in Fig. 12 for changing the secondary control parameter of the follower $\text{DER}_{1,2}$, i.e., τ, in [0.1, 5] s. According to Fig. 12(a), the IMGs are asymptotically stable for $0.1\text{ s}\leq\tau\leq 2.4$ s, and according to Fig. 11(b), they cannot be stable for any value of τ in the range due to nonzero PCC voltage differences, i.e., $\Delta V_{pcc,d}=\pm 5$ V.

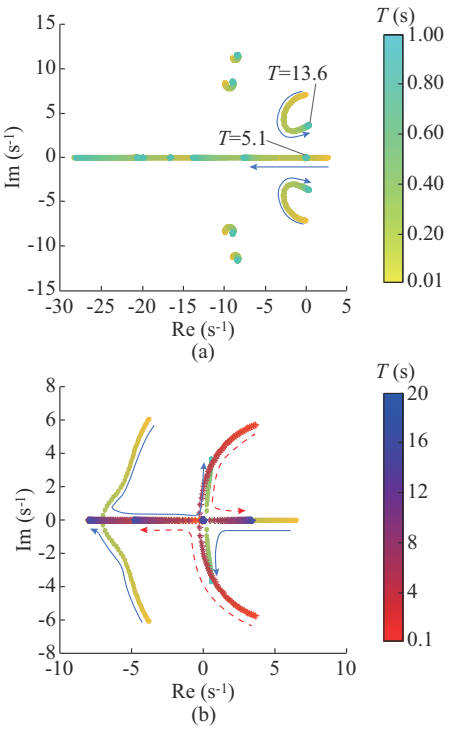

Fig. 11. Loci of dominant eigenvalues of IMGs. (a) All PCC voltage and frequency differences are zero. (b) $\Delta V_{pcc,d}=-5$ V for circles and $\Delta V_{pcc,d}=5$ V for stars.

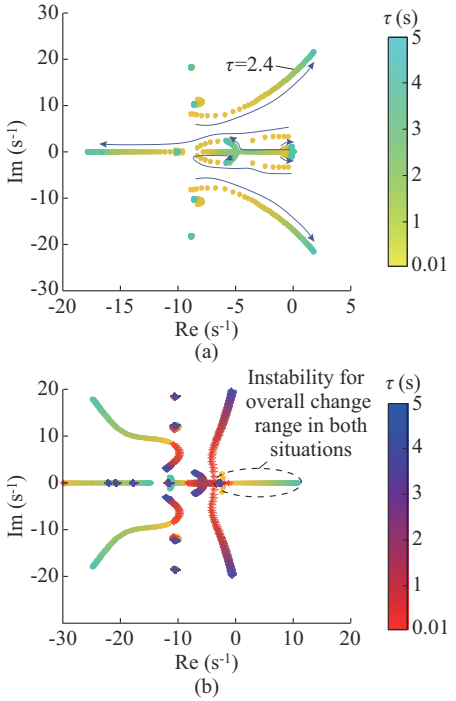

Fig. 12. Loci of dominant eigenvalues of IMGs under study for secondary control parameter of follower τ varying within [0.1, 5]s. (a) All PCC voltage and frequency differences are zero. (b) $\Delta V_{pcc,d}=-5$ V for circles and $\Delta V_{pcc,d}=5$ V for stars.

V. Transient Stability Assessment

Two nonlinear models are used for transient stability assessment. In Section V-A, we describe how a simplified nonlinear model of the exchanging power as presented in (5) is used to demonstrate power transitions during synchronization. In Section V-B, we explain how a detailed nonlinear model of the IMGs is used in SimPowerSystems/MATLAB to investigate the synchronization stability challenges under the time domain.

A. Transition During Synchronization

Section II described our investigation of the behavior of inrush power under variations in parameters. Next, the entire transition from pre-synchronization to disconnection of the synchronization control is considered. Figure 13 shows the active power exchange of the two IMGs under study versus the PCC phase difference during and after synchronization for the PCC voltage and frequency differences. The system operating points before and after synchronization are obtained from a simulation of successful synchronization using the control loops described in Section III-B. During pre-synchronization, the synchronization controller attempts to reduce $\Delta\phi_{pcc}$ to a pre-defined value or based on a certain constraint, where the exchange power is the inrush power (black solid line). During the control process, the inrush power may experience different routes of modification to achieve the scheduled power after synchronization (red dashed line). The route depends on the new operating point (i.e., the scheduled power amount). Routes ① and ② represent power exchanges from MG_2 to MG_1 and from MG_1 to MG_2, respectively. The routes are not necessarily for fixed voltage and frequency differences, as the control loops are regularly altering their characteristics to meet the new operating point. Therefore, different routes from the point ⓐ to the point ⓑ may occur according to the control parameters and length of the inrush power. Finally, the disconnection of the synchronization control leads to the power variations required to satisfy the IMG power-sharing objective.

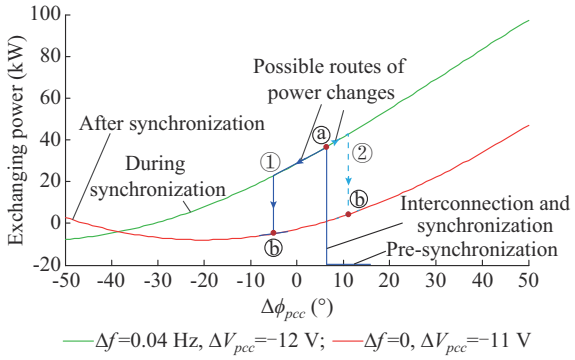

Fig. 13. Active power exchange of IMGs versus PCC phase difference during and after synchronization for PCC voltage and frequency differences.

A common synchronization used to enable a DER to connect to the grid is performed by zero-power generation to reduce the intensity of transients. Here, zero power exchange following IMG synchronization does not necessarily reduce the intensity of transients. Figure 13 shows that route ① produces intensive transients due to different directions of the power exchanges. However, route ② results in weaker transients. Besides, CB-IMG power exchange is not directly con-

trolled, as with BTBC-IMGs. In fact, IMG power-sharing control determines the amount of power exchange, which is embedded in the DER controllers. Therefore, an inevitable delay occurs in handling the power exchange, which causes it to be intermittent at the beginning of IMG formation. Moreover, unlike grid-connected MGs/DERs, the grid-feeding control strategy cannot be used for DERs during synchronization for direct control of the IMG power exchange due to the lack of a powerful frequency supporter, i.e., the main grid.

B. Time-domain Simulations

All simulations are obtained under zero initial conditions for all variables except the frequency, which is initiated at 50 Hz. The order of control/switching actions is as follows. First, the MGs are operated in an autonomous mode. Pre-synchronization control is then initiated prior to synchronization and interconnection. Interconnection is achieved by closing the CB. Finally, the pre-synchronization control loop is opened, and the MGs are operated as synchronous IMGs.

1) Trade-off Between Synchronization Control Objectives

The IMGs under study are autonomously operated prior to $t=5$ s. Pre-synchronization is initiated at $t=3$ s, that is, two seconds prior to the interconnection time of $t=5$ s. Synchronization control is fully disconnected at $t=7$ s. Figure 14(a) and (b) shows the PCC phase and voltage magnitude differences, respectively. The phase difference is considerable. However, the voltage magnitude difference is insignificant due to the MG operating conditions. Although pre-synchronization decreases the phase difference to 3° prior to synchronization, it produces a difference between the frequencies as shown in Fig. 14(c). This is because both phase and frequency errors are applied to the frequency control loop. Therefore, both frequency waveform and inrush power minimization should be considered for tuning the phase difference constraint during pre-synchronization.

Figure 15(a) and (b) shows the active and reactive power exchanged between IMGs, respectively. The synchronization is stable and the transients are smooth. However, they can be reduced using synchronization algorithms [20], [24], [28]. The steady-state values are tracked following disconnection of synchronization control. Figure 16(a) and (b) shows the active and reactive power sharing of DERs in isolated MGs and IMGs, respectively, before, during, and after synchronization. Although power sharing is affected by synchronization control, it remains stable, and active power sharing is well performed following synchronization disconnection.

2) Effects of Constraints on Synchronization Transients

As discussed in Sections II and V-B-1), the PCC frequency and phase differences are more effective for synchronization transients, and a trade-off is required in their minimization. Here, a simple algorithm is considered for applying the required constraints of synchronization, that is, $|\Delta f| \le \Delta f_{Thr}$, $|\Delta\phi_{pcc}| \le \Delta\phi_{Thr}$, and $|\Delta V_{pcc}| \le \Delta v_{Thr}$ conducted simultaneously, where Δf_{Thr}, $\Delta\phi_{Thr}$, and Δv_{Thr} are the frequency, phase, and voltage thresholds, respectively. Table IV lists the threshold values for the five scenarios. Scenarios 1, 3, and 4 are based on the trade-off between PCC frequency and phase differences. Scenario 2 is assumed to be the best constraint with both the low phase and frequency thresholds. Scenario 5 is the easiest constraint to satisfy, having large phase and frequency thresholds.

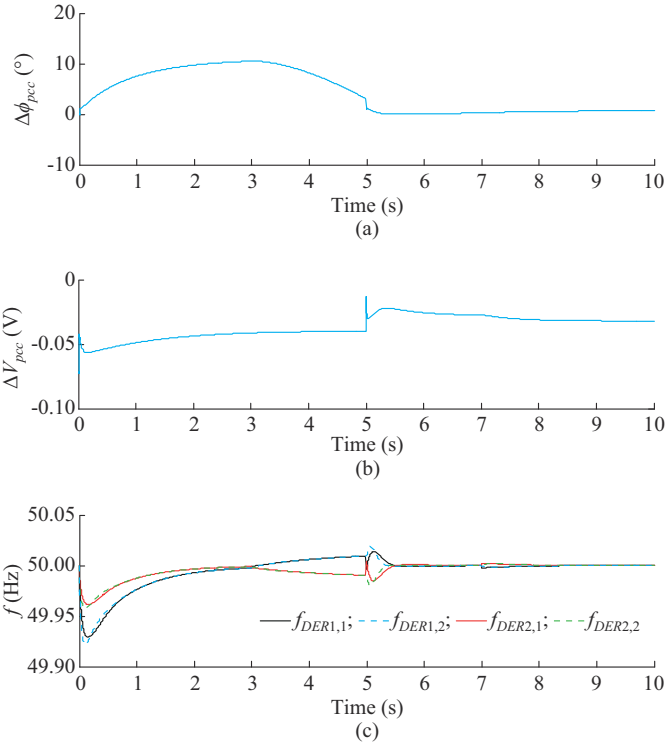

Fig. 14. Synchronization signals before, during, and after process. (a) PCC phase difference. (b) Voltage magnitude difference. (c) Frequency differences of PCCs.

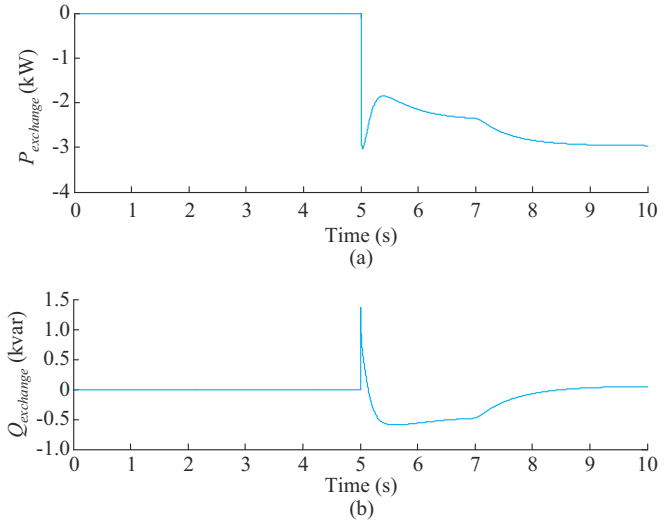

Fig. 15. Power exchanged between MGs before, during, and after synchronization. (a) Active power $P_{exchange}$. (b) Reactive power $Q_{exchange}$.

Figure 17(a) and (b) shows the active and reactive power exchanged between MGs for different synchronization constraints in scenarios specified in Table IV, respectively. Scenario 2 has the smoothest transients during synchronization. The algorithm can satisfy both thresholds even though both thresholds are small. Nevertheless, these small thresholds

may not be satisfied under a difficult condition such as a high load.

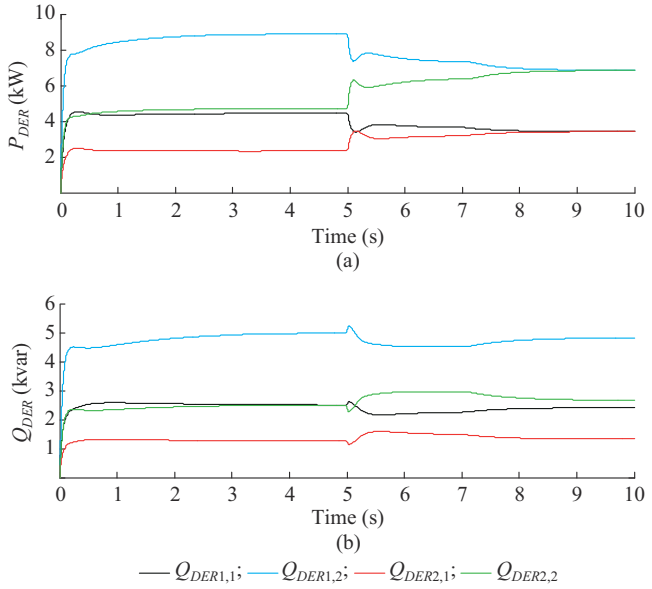

Fig. 16. Power sharing of DERs in isolated MGs and IMGs before, during, and after synchronization. (a) Active power P_{DER}. (b) Reactive power Q_{DER}.

TABLE IV
THRESHOLD VALUES FOR FIVE SCENARIOS

Scenario	Δf_{Thr} (Hz)	$\Delta\phi_{Thr}$ (°)
1	0.01	7
2	0.02	2
3	0.03	5
4	0.05	3
5	0.10	10

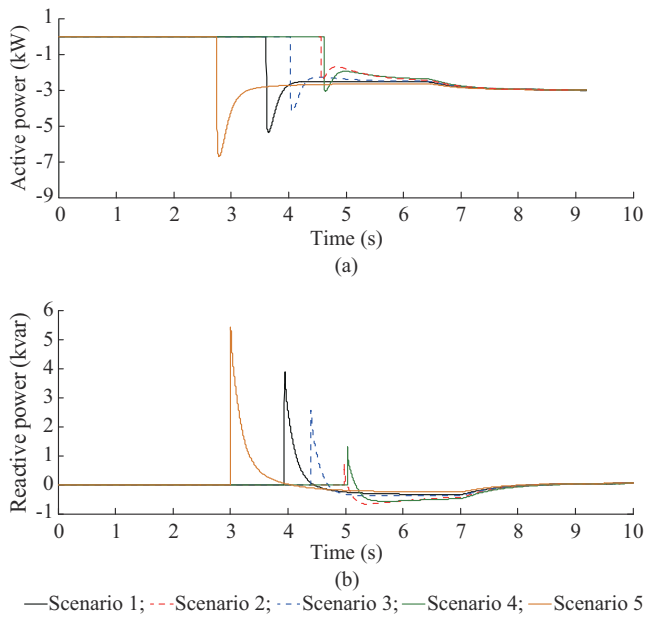

Fig. 17. Power exchanged between MGs for different synchronization constraints in scenarios specified in Table IV. (a) Active power. (b) Reactive power.

3) Synchronization During High-load MGs

Here, the MG loads increase by twice that of the basic loads; that is, under a high-load condition. Pre-synchronization is initiated at $t=3$ s, and two constraints are considered: $\Delta f=0.1$ Hz, $\Delta\phi_{pcc}=10°$ and $\Delta f=0.02$ Hz, $\Delta\phi_{pcc}=2°$. Figure 18(a) shows the frequencies of the leader DERs for both constraints, where high transient states are present, particularly with the first constraint. Although both scenarios of constraints are stable in the steady state, the rate of change of frequency is high during transients. Therefore, the operation may be interrupted by protection devices. Note that inverter-based DERs lead to very low inertia [3], which makes the IMG frequency vulnerable to disturbances. Figure 18(b) shows the active power exchange between MGs, where large transients can also be observed. The MG voltage/frequency is severely affected by these transients of exchanged powers.

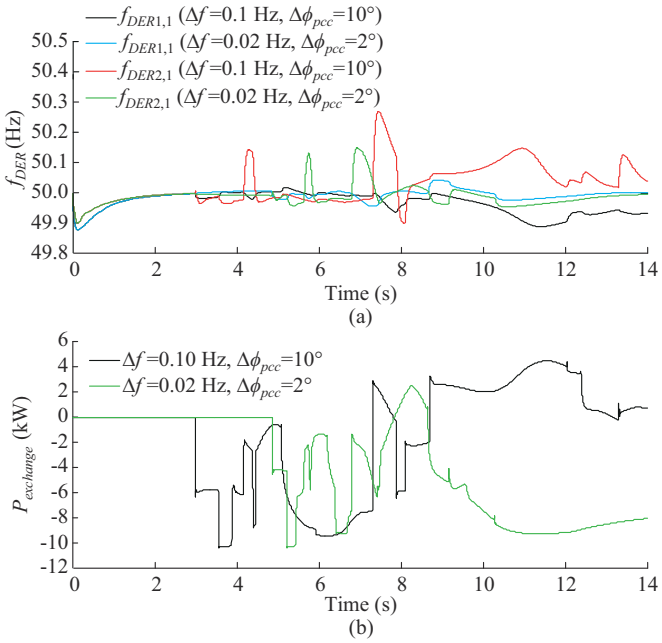

Fig. 18. Synchronization under high-load conditions. (a) Frequency of leader DERs f_{DER}. (b) $P_{exchange}$.

Although transient stability is satisfied for low MG loads and various thresholds of synchronization constraints within the limitations of IEEE Standard 1547, which are described in Sections V-B1 and V-B2, a high-load condition causes synchronization with inappropriate transients. This is true even for thresholds lower than the limitations represented in IEEE Standard 1547 criteria, which can also lead to instability. Therefore, the allowable thresholds that are represented in IEEE Standard 1547 must be modified for the synchronization of weak IMGs.

VI. CONCLUSION

In this paper, the synchronization stability of IMGs is investigated through small-signal analysis and transient stability assessment. Inrush power plays a critical role in synchronization stability, which is mostly affected by the frequency and phase differences of the interconnection points of the MGs, i.e., the ends of the interlinking line. In addition, low-

voltage MGs with low *X/R* ratios of interlinking lines have lower active but greater reactive inrush power. However, lower line impedances lead to greater active and reactive inrush power. The transition from inrush to scheduled power is discussed, where the amplitudes of the transient states represent a random variable that is dependent on the inrush and scheduled power values and controller gains. Nevertheless, because the usual values of the scheduled power are less than the usual values of the inrush power, achieving lower inrush power is generally a reasonable objective. Nonzero voltage/phase/frequency differences may lead to small-signal instability at the primary operation point, and the synchronization can only be small-signal stable for zero differences. The stabilizing ranges of the control gains are calculated for the synchronization, and secondary controllers are the significant controllers for synchronization stability. Studies have shown that lower thresholds of the synchronization controller result in lower transients. The transient stability is satisfied for low-load conditions and different thresholds of synchronization constraints. Nevertheless, high-load operations lead to synchronization with higher transient states, particularly for large thresholds that are still less than those of the IEEE Standard 1547 criteria, which can also cause instability. These results reveal the limitations of the IEEE Standard 1547. Accordingly, the standard should be revised for synchronization of weak MGs during interconnections.

REFERENCES

[1] C. Chen, J. Wang, F. Qiu *et al.*, "Resilient distribution system by microgrids formation after natural disasters," *IEEE Transactions on Smart Grid*, vol. 7, no. 2, pp. 958-966, Mar. 2016.

[2] M. Shahidehpour, Z. Li, S. Bahramirad *et al*., "Networked microgrids: exploring the possibilities of the IIT-bronzeville grid," *IEEE Power and Energy Magazine*, vol. 15, no. 4, pp. 63-71, Aug. 2017.

[3] M. Naderi, Q. Shafiee, H. Bevrani *et al*., "Low-frequency small-signal modeling of interconnected AC microgrids," *IEEE Transactions on Power Systems*, vol. 36, no. 4, pp. 2786-2797, Jul. 2020.

[4] X. Wu, Y. Xu, J. He *et al*., "Pinning-based hierarchical and distributed cooperative control for ac microgrid clusters," *IEEE Transactions on Power Electronics*, vol. 35, no. 9, pp. 9867-9887, Sept. 2020.

[5] S. Weng, Y. Xue, J. Luo *et al*., "Distributed secondary control for islanded microgrids cluster based on hybrid-triggered mechanisms," *Processes*, vol. 8, no. 3, p. 370, Mar. 2020.

[6] X. Lu, J. Lai, and X. Yu, "A novel secondary power management strategy for multiple AC microgrids with cluster-oriented two-layer cooperative framework," *IEEE Transactions on Industrial Informatics*, vol. 17, no. 2, pp. 1483-1495, Feb. 2020.

[7] I. P. Nikolakakos, H. H. Zeineldin, M. S. El-Moursi *et al*., "Stability evaluation of interconnected multi-inverter microgrids through critical clusters," *IEEE Transactions on Power Systems*, vol. 31, no. 4, pp. 3060-3072, Jul. 2016.

[8] M. Batool, F. Shahnia, and S. M. Islam, "Multi-level supervisory emergency control for operation of remote area microgrid clusters," *Journal of Modern Power Systems and Clean Energy*, vol. 7, no. 5, pp. 1210-1228, Sept. 2019.

[9] M. Naderi, Y. Khayat, Q. Shafiee *et al*., "Interconnected autonomous ac microgrids via back-toback converters – part I: small-signal modeling," *IEEE Transactions on Power Electronics*, vol. 35, no. 5, pp. 4728-4740, May 2019.

[10] M. Naderi, Y. Khayat, Q. Shafiee *et al*., "Interconnected autonomous ac microgrids via back-to-back converters – part II: stability analysis," *IEEE Transactions on Power Electronics*, vol. 35, no. 11, pp. 11801-11812, Nov. 2020.

[11] B. John, A. Ghosh, M. Goyal *et al*., "A DC power exchange highway based power flow management for interconnected microgrid clusters," *IEEE Systems Journal*, vol. 13, no. 3, pp. 3347-3357, Sept. 2019.

[12] N. Jaalam, N. Rahim, A. Bakar *et al*., "A comprehensive review of synchronization methods for grid-connected converters of renewable energy source," *Renewable and Sustainable Energy Reviews*, vol. 59, pp. 1471-1481, Jun. 2016.

[13] M. Litwin, D. Zieliński, and K. Gopakumar, "Remote micro-grid synchronization without measurements at the point of common coupling," *IEEE Access*, vol. 8, pp. 212753-212764, Nov. 2020.

[14] M. G. Taul, X. Wang, P. Davari *et al*., "An overview of assessment methods for synchronization stability of grid-connected converters under severe symmetrical grid faults," *IEEE Transactions on Power Electronics*, vol. 34, no. 10, pp. 9655-9670, Oct. 2019.

[15] X. Wang, M. G. Taul, H. Wu *et al*., "Grid-synchronization stability of converter-based resources – an overview," *IEEE Open Journal of Industry Applications*, vol. 1, pp. 115-134, Aug. 2020.

[16] S. I. Nanou and S. A. Papathanassiou, "Grid code compatibility of VSC-HVDC connected offshore wind turbines employing power synchronization control," *IEEE Transactions on Power Systems*, vol. 31, no. 6, pp. 5042-5050, Nov. 2016.

[17] A. Pasha, M. S. El-Moursi, H. H. Zeineldin *et al*., "Enhanced transient response and seamless interconnection of multi-microgrids based on an adaptive control scheme," *IET Renewable Power Generation*, vol. 15, no. 11, pp. 2452-2467, Apr. 2021.

[18] T. L. Vandoorn, B. Meersman, J. D. de Kooning *et al*., "Transition from islanded to grid-connected mode of microgrids with voltage-based droop control," *IEEE Transactions on Power Systems*, vol. 28, no. 3, pp. 2545-2553, Aug. 2013.

[19] X. Hou, Y. Sun, J. Lu *et al*., "Distributed hierarchical control of ac microgrid operating in grid-connected, islanded and their transition modes," *IEEE Access*, vol. 6, pp. 77388-77401, Nov. 2018.

[20] M. A. Ebrahim, B. A. A. Ayoub, M. N. F. Nashed *et al*., "A novel hybrid-HHOPSO algorithm based optimal compensators of fourlayer cascaded control for a new structurally modified AC microgrid," *IEEE Access*, vol. 9, pp. 4008-4037, Dec. 2020.

[21] F. Tang, J. M. Guerrero, J. C. Vasquez *et al*., "Distributed active synchronization strategy for microgrid seamless reconnection to the grid under unbalance and harmonic distortion," *IEEE Transactions on Smart Grid*, vol. 6, no. 6, pp. 2757-2769, Nov. 2015.

[22] D. Shi, X. Chen, Z. Wang *et al*., "A distributed cooperative control framework for synchronized reconnection of a multi-bus microgrid," *IEEE Transactions on Smart Grid*, vol. 9, no. 6, pp. 6646-6655, Nov. 2017.

[23] G. G. Talapur, H. M. Suryawanshi, L. Xu *et al*., "A reliable microgrid with seamless transition between grid connected and islanded mode for residential community with enhanced power quality," *IEEE Transactions on Industry Applications*, vol. 54, no. 5, pp. 5246-5255, Sept. 2018.

[24] Y. Sun, C. Zhong, X. Hou *et al*., "Distributed cooperative synchronization strategy for multi-bus microgrids," *International Journal of Electrical Power & Energy Systems*, vol. 86, pp. 18-28, Mar. 2017.

[25] B. E. Sedhom, M. M. El-Saadawi, A. Y. Hatata *et al*., "H-infinity versus model predictive control methods for seamless transition between islanded- and grid-connected modes of microgrids," *IET Renewable Power Generation*, vol. 14, no. 5, pp. 856-870, Aug. 2020.

[26] L. Xia and L. Hai, "A seamless transfer strategy based on multi-master and multi-slave microgrid," in *Proceedings of 9th IEEE International Symposium Power Electronics for Distributed Generation Systems (PEDG)*, Vakncia, Spain, Aug. 2018, pp. 1-5.

[27] *IEEE Standard for Interconnection and Interoperability of Distributed Energy Resources with Associated Electric Power Systems Interfaces*, IEEE Standard 1547™, 2018.

[28] F. Shahnia and S. Bourbour, "A practical and intelligent technique for coupling multiple neighboring microgrids at the synchronization stage," *Sustainable Energy, Grids and Networks*, vol. 11, pp. 13-25, Sept. 2017.

[29] N. Bilidis, "Seamless transitions of multiple micro-grids between the backbone interconnected and the islanded operational modes," M. S. thesis, Department of Electric and Sustainable Energy, Delft University of Technolgy, Delft, The Netherlands, Aug. 2016.

[30] S. Kim, "Experimental verification for seamless mode transitions of multiple microgrids using fuzzy-based droop controller," M. S. thesis, Department of Electric and Sustainable Energy, Delft University of Technolgy, Delft, The Netherlands, Oct. 2017.

[31] IEEE Dataport. (2022, Sept.). Dataset for synchronization stability of interconnected MGs. [Online]. Available: https://dx. doi. org/10.21227/ve77-ct59

[32] W. Liu, W. Gu, Y. Xu *et al*., "General distributed secondary control for multi-microgrids with both PQ-controlled and droop-controlled distributed generators," *IET Generation, Transmission & Distribution*,

vol. 11, no. 3, pp. 707-718, Feb. 2017.
[33] L. Ren, Y. Qin, Y. Li *et al*., "Enabling resilient distributed power sharing in networked microgrids through software defined networking," *Applied Energy*, vol. 210, pp. 1251-1265, Jan. 2018.
[34] J. Lai, X. Lu, X. Yu *et al*., "Cluster-oriented distributed cooperative control for multiple ac microgrids," *IEEE Transactions on Industrial Informatics*, vol. 15, no. 11, pp. 5906-5918, Nov. 2019.
[35] X. Wu, Y. Xu, X. Wu *et al*., "A two-layer distributed control method for islanded networked microgrid systems," *IEEE Transactions on Smart Grid*, vol. 11, no. 2, pp. 942-957, Mar. 2019.
[36] J. He, X. Wu, X. Wu *et al*., "Small-signal stability analysis and optimal parameters design of microgrid clusters," *IEEE Access*, vol. 7, pp. 36896-36909, Feb. 2019.
[37] M. Naderi, Y. Khayat, Q. Shafiee *et al*., "Comprehensive small-signal modeling and Prony analysis-based validation of synchronous interconnected microgrids," *Energy Reports*, vol. 7, pp. 6677-6689, Nov. 2021.

Mobin Naderi received the B.Sc., M.Sc. and Ph.D. degrees in electrical engineering from Tabriz University, Tabriz, Iran, Iran University of Science and Technology, Tehran, Iran, and University of Kurdistan, Sanandaj, Iran, in 2012, 2014, and 2019, respectively. He was a Visiting Ph.D. Student with Department of Energy Technology, Aalborg University, Aalborg, Denmark. He is now a Postdoctoral Researcher at University of Kurdistan. His research interests include modeling, stability analysis and control of autonomous/interconnected microgrids, and robust control methods.

Qobad Shafiee received the Ph.D. degree in electrical engineering from the Department of Energy Technology, Aalborg University, Aalborg, Denmark, in 2014. He is currently an Assistant Professor, Director of International Affairs, and Co-Leader of the Smart/Micro Grids Research Center at the University of Kurdistan, Sanandaj, Iran, where he was a Lecturer from 2007 to 2011. In 2014, he was a Visiting Scholar with the Electrical Engineering Department, the University of Texas at Arlington, Arlington, USA. He was a Post-Doctoral Fellow with the Department of Energy Technology, Aalborg University, in 2015. His current research interests include modeling, energy management, control of power electronics-based systems and microgrids, and model predictive and optimal control of modern power systems.

Frede Blaabjerg was with ABB-Scandia, Randers, Denmark, from 1987 to 1988. From 1988 to 1992, he received the Ph.D. degree in electrical engineering at Aalborg University, Aalborg, Denmark, in 1995. He became an Assistant Professor in 1992, an Associate Professor in 1996, and a Full Professor of power electronics and drives in 1998. From 2017 he became a Villum Investigator. He is honoris causa at University Politehnica Timisoara (UPT), Timisoara, Romania, and Tallinn Technical University (TTU), Tallinn, Estonia. He has published more than 600 journal papers in the fields of power electronics and its applications. He is the co-author of four monographs and editor of ten books in power electronics and its applications. He has received 32 IEEE Prize Paper Awards, the IEEE PELS Distinguished Service Award in 2009, the EPE-PEMC Council Award in 2010, the IEEE William E. Newell Power Electronics Award 2014, the Villum Kann Rasmussen Research Award 2014 and the Global Energy Prize in 2019. He was the Editor-in-Chief of the IEEE Transactions on Power Electronics from 2006 to 2012. He has been Distinguished Lecturer for the IEEE Power Electronics Society from 2005 to 2007 and for the IEEE Industry Applications Society from 2010 to 2011 as well as 2017 to 2018. In 2019-2020 he serves a President of IEEE Power Electronics Society. He is Vice-President of the Danish Academy of Technical Sciences too. He is nominated in 2014-2018 by Thomson Reuters to be between the most 250 cited researchers in Engineering in the world. His current research interests include power electronics and its applications such as in wind turbines, PV systems, reliability, harmonics and adjustable speed drives.

Hassan Bevrani received the Ph. D. degree in electrical engineering from Osaka University, Osaka, Japan, in 2004. Currently, he is a Full Professor and the Program Leader of Smart/Micro Grids Research Center (SMGRC) at the University of Kurdistan (UOK), Sanandaj, Iram. From 2016 to 2019, he was the UOK Vice-chancellor for research and technology. Over the years, he has worked as Senior Research Fellow and Visiting Professor with Osaka University, Osaka, Japan, Kumamoto University, Kumamoto, Japan, Queensland University of Technology, Brisbane, Australia, Kyushu Institute of Technology, Kitakyushu, Japan, Centrale Lille, Lille, France, and Technical University of Berlin, Berlin, Germany. He is the author of 6 international books, 15 book chapters, and more than 300 journal/conference papers. His current research interests include smart grid operation and control, power systems stability and optimization, microgrid dynamics and control, and Intelligent/robust control applications in power electric industry.